Spectral Characterization of Optical Aberrations in Fluidic Lenses

GRACIANA PUENTES[1,2,*] AND FERNANDO MINOTTI[1,3]

[1] *Universidad de Buenos Aires. Facultad de Ciencias Exactas y Naturales. Departamento de Física. Buenos Aires, Argentina*
[2] *CONICET-Universidad de Buenos Aires. Instituto de Física de Buenos Aires (IFIBA). Buenos Aires, Argentina*
[3] *CONICET-Universidad de Buenos Aires. Instituto de Física Interdisciplinaria y Aplicada (INFINA). Buenos Aires, Argentina.*
[*] *gpuentes@df.uba.ar*

Abstract: We report an extensive numerical study and supporting experimental results on the spectral characterization of optical aberrations in macroscopic fluidic lenses with tunable focal distance and aperture shape. Using a Shack-Hartmann wave-front sensor we experimentally reconstruct the near-field wave-front transmitted by the fluidic lenses, and we characterize the chromatic aberrations in terms of Zernike polynomials in the visible range. Moreover, we further classify the spectral response of the lenses using clustering techniques, in addition to correlation and convolution measurements. Experimental results are in agreement with our theoretical model of the non-linear deformation of thin elastic membranes.

© 2023 Optica Publishing Group

References

1. D. A. Goss and R. W. West, "Introduction to the Optics of the Eye" (Butterworth-Hienemann, 2001).
2. M. P. Keating, Geometric, "Physical and Visual Optics" (Butterworth-Hienemann, 2002).
3. W. Tasman and E. A. Jaeger, "Duane's Ophtalmology" (LLW, 2013).
4. T. Callina and T. P. Reynolds, "Traditional methods for the treatment of presbyopia: spectacles, contact lenses, bifocal contact lenses", Ophthalmol. Clin. North Am. **19**, 25-33 (2006).
5. Patent Application WO2006011937A2, "Fluidic Adaptive Lens".
6. N. Hazan, A. Banerjee, H. Kim, C. Mastrangelo, "Tunable-focus lens for adaptive eyeglasses", Opt. Express **25**, 1221 (2017).
7. O. Takayama, F. Minotti, G. Puentes, "Tunable Fluidic Lenses with High Dioptric Power", OSA Continuum **1**, 181 (2018).
8. G. Puentes, D. Voigt, A. Aiello and J. P. Woerdman, "Experimental observation of depolarized light scattering", Opt. Lett. **30**, 3216-3219 (2005).
9. G. Puentes Invention Disclosure Nr.20170102760. "Adaptive Fluidic Lenses for Subnormal Vision Segment" (TCPind0335-01).
10. F. Schneider, J. Draheim, R. Kamberger, U. Wallrabe, Process and material properties of polydimethylsiloxane (PDMS) for Optical MEMS, Sensor and Actuators A **151**, 95-99 (2006).
11. M. Vallet, B. Berge, and L. Vovelle, "Electrowetting of water and aqueos solutions on poly-ethilene-terephthalate insulating films", Polymer **37**, 2465-2470 (1996).
12. T. Krupenking, S. Yang, P. Mach, "Tunable liquid microlens", Appl. Phys. Lett. **82**, 316-318 (2003).
13. S. Kuiper andB. H. Hendriks, "Variable-focus liquid lens for miniature cameras", Appl. Phys. Lett. **85**, 1128-1130 (2004).
14. G. C. Knollman, J. L. Bellini, J. L. Weaver, "Variable-focus liquid-filled hydroacoustic lens", J. Acoust. Soc. Am. **49**, 253-261 (1971).
15. N. Sigiura and S. Morita, "Variable-docus liquid-filled optics lens", App. Opt. **32**, 4181-4186 (1993).
16. D. Y. Zhang, V. Lien, Y. Berdichevsky, J. Choi, and Y. H. Lo, "Fluidic adaptivelens with high focal length tenability", App. Phys. Lett. **82**, 3171-3172 (2003).
17. K. H. Joeng, G. L. Liu, N. Chronis, And L. P. Lee, "Tunable microdoublets lens array", Opt. Express **12**, 2494-2500 (2004).
18. J. Chen, W. Wang, J. Fang, and K. Varahramyan, "Variable focusing microlens with microfluidic chip", J. Micromech. Microeng. **14**. 675-680 (2004).

19. N. Chronis, G. L. Liu, K. H. Jeong, and L. P. Lee, "Tunable liquid filled micro-lens array integrated with microfludidic network", Opt. Express **11**, 2370-2378 (2003).
20. P. M. Moran, s. Dharmatilleke, A. H. Khaw, and K. W. Tan, “Fluid lenses with variable focal length”, App. Phys. Lett. **88**, 041120 (2006).
21. H. Ren and S-T Wu, “Variable-focus liquid lens”, Opt. Express **15**, 5931-5936 (2007).
22. N. A. Polson, and M. A. Hayes, “Microfluidics controllling fluids in small places”, Anal. Chem. **73**, 312A-319A (2001).
23. E. Hetch, Optics, 2nd Ed. (Addison Wesley, NY, 2002).
24. H. M. Beger, “A new approach to the analysis of large deflections of plates”, J. Appl. Mech. **22**, 1955, pp. 465-472.
25. J. Mazumdar, “A method for solving problems of elastic plates of arbitrary shape”, J. Aust. Math. Soc. **XI**, 1970, pp. 95-112.
26. J. Mazumdar and R. Jones, “A simplified approach to the analysis of large deflections of plates”, J. Appl. Mech. **41**, 1974, pp. 523-524.
27. Raw experimental data and numerical simulations are availble at our Github repository https://github.com/grapts/Fluidic-Lenses-Data

Introduction

One of the most common ocular disorders worldwide, and the main cause of visual impairment in children, is myopia. The elongation of the axial length in the eyes which characterizes medium and high levels of myopia can increase the risk of severe ocular pathologies, potentially leading to irreversible blindness. Most traditional adaptive eye-wear based on fluidic lenses aim to correct refractive errors requiring medium dioptric power, such as mild myopia, hyperopia, an other focus errors [5, 6]. On the other hand, refractive errors other than focus, including coma, astigmatism and higher order aberrations are usually treated via astigmatic corrections [1–3], which are more difficult to achieve with standard fluidic lenses. Moreover, in most cases compounded errors are present, most commonly presbyopia with focus defects, requiring multi-focal lenses whose limited accommodation distance and highly restricted field-of-view can lead to high loss of visual capacity [4]. Finally, those patients with severe visual impairment due to glaucoma or other visual traumas, require large dioptric power corrections, necessitating thick organic lenses, which are prone to high-order aberrations, in addition to being significantly unattractive and unpractical. In a previous publication [7], we presented the first macroscopic fluidic lens eye-wear prototype with high dioptric power (+25D to +100D range) with optical aberrations below a fraction of the wavelength, which can adaptively restore accommodation distance within several centimeters, thus enabling access to the entire field-of-view. The lens is made of an elastic polymer of the PDMS type which can adaptively modify its optical power according to the fluidic volume mechanically pumped in. Such liquid lens exhibits a large dynamic range, and its focusing properties are polarization independent [8]. Additionally, we demonstrated that by tuning the lens aperture it is possible to address different optical aberrations, thus providing an additional degree of freedom for the lens design. Our design is attractive for adaptive eye-wear, in addition to cellular phone, camera, optical zooms, or other machine vision applications where large magnification can be required [9].

In this paper, we present an extensive numerical and experimental spectral study of optical aberrations in macroscopic fluidic lenses with high dioptric power, tunable focal distance and aperture shape [7], based on an empirical characterization of the refractive index of thin elastic membranes, such as PDMS, according to the Sellmeier model [10]. Using a Shack-Hartmann wave-front sensor we experimentally reconstruct the near-field wave-front transmitted by such fluidic lenses, and we characterize the chromatic aberrations in terms of Zernike polynomials over the visible wavelength range ($\lambda = 400 - 650$ nm), using a programmable LED source. Moreover, we further classify the spectral response of the lenses using clustering techniques, in addition to correlation and convolution measurements. Experimental results are in agreement with our theoretical model of the non-linear elastic membrane deformation.

1. Theoretical model

1.1. Inclusion of gravity effects

We briefly recall the model used in [7] to simulate the fluid lens surface shape without considering gravity effects.The equations used are those derived by Berger [24] to determine the nonlinear, large deformation of thin isotropic elastic plates:

$$\nabla^4 w - \alpha^2 \nabla^2 w = \frac{q}{D}, \tag{1a}$$

$$\frac{\partial u}{\partial x} + \frac{\partial v}{\partial y} + \frac{1}{2}\left(\frac{\partial w}{\partial x}\right)^2 + \frac{1}{2}\left(\frac{\partial w}{\partial y}\right)^2 = \frac{\alpha^2 h^2}{12}. \tag{1b}$$

In these equations $w(x, y)$ is the local z-displacement of the membrane, with non-deformed state assumed to correspond to the $z = 0$ plane, $u(x, y)$ and $v(x, y)$ are the local x and y displacements, D the membrane bending rigidity, and h its thickness. The magnitude $q(x, y)$ corresponds to the applied z-load, and α is a constant to be determined from the same equations by imposing appropriate boundary conditions.

For the case of uniform load (constant q) and elliptic aperture, analytical solutions of the system (1) were obtained by the method of constant deflection contour lines derived by Mazumdar [25]. If the aperture in the plane $z = 0$ is an ellipse of x, y semiaxes a and b, respectively, the z-displacement of the membrane is given by

$$w(\varsigma) = \frac{\Delta V}{\pi a b} \frac{2\gamma\left[\gamma\left(1-\varsigma^2\right) I_1(2\gamma) + I_0(2\gamma\varsigma) - I_0(2\gamma)\right]}{\left(\gamma^2+2\right) I_1(2\gamma) - 2\gamma I_0(2\gamma)}. \tag{2}$$

where ΔV is the volume of the liquid, the variable ς is defined as

$$\varsigma^2 = x^2/a^2 + y^2/b^2, \tag{3}$$

and the constant γ is related to ΔV by

$$\Delta V = \pi a b h \frac{\sqrt{3a^4 + 2a^2b^2 + 3b^4}}{a^2+b^2} G(\gamma), \tag{4}$$

where

$$G(\gamma) = \frac{\left(\gamma^2+2\right) I_1(2\gamma) - 2\gamma I_0(2\gamma)}{\sqrt{24\gamma}\sqrt{3\gamma\left[I_1(2\gamma)\right]^2 - 2I_2(2\gamma)\left[\gamma I_0(2\gamma) + 2I_1(2\gamma)\right]}}. \tag{5}$$

We consider now the effect of gravity when the (x, y) plane of the lens aperture is vertical. In Berger equations (1) the load q has now the expression

$$q = q_0 - \rho g\left(x\sin\theta + y\cos\theta\right),$$

with q_0 the load at the lens center ($x = y = 0$), ρ the mass density of the filling fluid, g the acceleration of gravity, and θ the angle between the vertical direction and the y axis (see figure 1).

In the case that $\rho g L/q_0 \ll 1$, with L a characteristic length of the lens pupil, we can treat gravity effects as a perturbation to the case with uniform load q_0, previously obtained, and write

$$\begin{aligned} w &= w_0 + w_1, \\ \alpha &= \alpha_0 + \alpha_1, \end{aligned}$$

with w_0 and α_0 corresponding to the solution of the case with $q = q_0$. Linearization of Eq. (1a) in the perturbations w_1 and α_1 yields

$$\nabla^4 w_1 - \alpha_0^2 \nabla^2 w_1 - 2\alpha_0\alpha_1\nabla^2 w_0 = -\frac{\rho g}{D}\left(x\sin\theta + y\cos\theta\right), \tag{6}$$

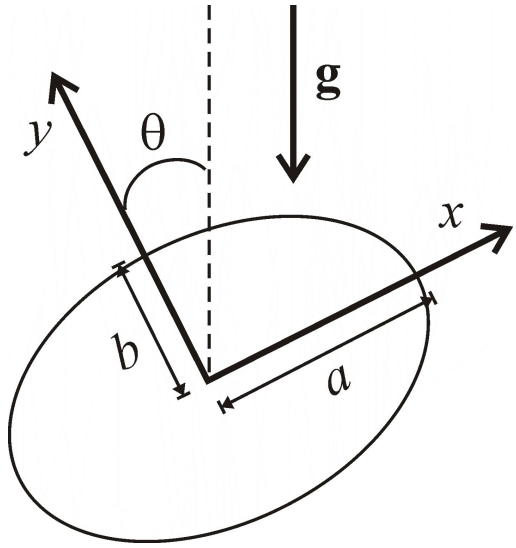

Fig. 1. Notation used in the model to include the effect of gravity on the lens surface shape.

For a clamped membrane with no pre-stretching $u = v = 0$ at $\psi = 0$, and so the integral of the linearized version of Eq. (1b) over the area S_0 of the lens aperture gives

$$\int_{S_0} \left(\frac{\partial w_0}{\partial x}\frac{\partial w_1}{\partial x} + \frac{\partial w_0}{\partial y}\frac{\partial w_1}{\partial y} \right) dxdy = \frac{\alpha_0 \alpha_1 h^2}{6} S_0. \tag{7}$$

We now consider the solution to Eq. (6) in the usual case in which the membrane forces dominate: $\alpha_0^2 L^2 \gg 1$. In this case, except extremely close to the membrane border, one has $\left|\nabla^4 w_1\right| \ll \left|\alpha_0^2 \nabla^2 w_1\right|$, and so it is easy to check that the solution to Eq. (6) satisfying the boundary condition $w_1 = 0$ at the border of the membrane is given by

$$w_1 = -\frac{2\alpha_1}{\alpha_0} w_0 - \frac{\rho g a^2 b^2}{2D\alpha_0^2} \left(1 - \frac{x^2}{a^2} - \frac{y^2}{b^2}\right) \left(\frac{x \sin\theta}{a^2 + 3b^2} + \frac{y \cos\theta}{3a^2 + b^2}\right). \tag{8}$$

Using expression (8) in Eq. (7) one readily obtains $\alpha_1 = 0$, so that the complete solution with the inclusion of gravity effects is

$$w = w_0 - \frac{\rho g}{2D\gamma^2} \frac{a^4 b^4 \left(a^2 + b^2\right)}{3a^2 + 2a^2 b^2 + 3b^4} \left(1 - \frac{x^2}{a^2} - \frac{y^2}{b^2}\right) \left(\frac{x \sin\theta}{a^2 + 3b^2} + \frac{y \cos\theta}{3a^2 + b^2}\right), \tag{9}$$

where w_0 is the solution previously obtained for uniform load, Eq. (2), and the constant γ is the one determined in that solution using Eq. (4).

1.2. Determination of the aberrations of the fluid lens

In order to determine the aberrations of a fluid lens with one plane surface we consider a plane wave front with normal incidence on the plane side of the membrane, taken at $z = 0$ (see figure 2). The corresponding rays, parallel to the z -axis, of unit vector $\mathbf{e}_z$, are then refracted according to Snell law when they cross the membrane curved surface at $z = w\,(x, y)$. The external normal

unit vector at that surface is given by (in Cartesian components)

$$\mathbf{n} = \frac{\left(-w_x, -w_y, 1\right)}{\sqrt{1 + w_x^2 + w_y^2}}, \tag{10}$$

where the subscripts x, y indicate derivatives with respect to the corresponding coordinate.

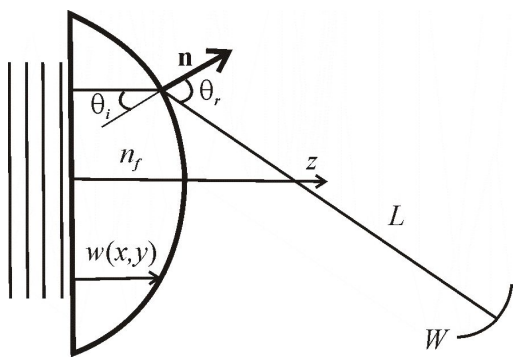

Fig. 2. Notation used in the model for the ray tracing from a plane wavefront incident on the plane surface of the lens to the refracted wavefront W

The angle θ_i of the rays incident from inside the lens, relative to the external normal direction at the corresponding point of the membrane curved surface, is thus given by

$$\cos\theta_i = \mathbf{n} \cdot \mathbf{e}_z = \frac{1}{\sqrt{1 + w_x^2 + w_y^2}}. \tag{11}$$

Snell law then determines the angle of the refracted ray emerging from the lens, also relative to the normal direction, as

$$\sin\theta_r = n_f \frac{\sqrt{w_x^2 + w_y^2}}{\sqrt{1 + w_x^2 + w_y^2}}, \tag{12}$$

where n_f is the index of refraction of the filling fluid, relative to that of air.

The refracted ray is contained in the plane determined by the normal unit vector $\mathbf{n}$ and the unit vector tangent to the surface

$$\mathbf{t} = \frac{\mathbf{e}_z - (\mathbf{n} \cdot \mathbf{e}_z)\,\mathbf{n}}{|\mathbf{e}_z - (\mathbf{n} \cdot \mathbf{e}_z)\,\mathbf{n}|} = \frac{\left(w_x, w_y, w_x^2 + w_y^2\right)}{\sqrt{\left(1 + w_x^2 + w_y^2\right)\left(w_x^2 + w_y^2\right)}}, \tag{13}$$

so that the ray direction is given by the unit vector

$$\mathbf{k}_r = \mathbf{n}\cos\theta_r + \mathbf{t}\sin\theta_r. \tag{14}$$

The explicit expressions of the Cartesian components of $\mathbf{k}_r$ are

$$k_{rx,y} = \frac{n_f - \sqrt{1 + \left(1 - n_f^2\right)\left(w_x^2 + w_y^2\right)}}{1 + w_x^2 + w_y^2} w_{x,y}, \tag{15a}$$

$$k_{rz} = \frac{n_f\left(w_x^2 + w_y^2\right) + \sqrt{1 + \left(1 - n_f^2\right)\left(w_x^2 + w_y^2\right)}}{1 + w_x^2 + w_y^2}, \tag{15b}$$

which are functions of the point (x, y) in the plane $z = 0$, at which the ray originated.

In this way, a generic ray starting at the point (x, y) in the plane $z = 0$ inside the lens is refracted at the point $\mathbf{X}_0 = (x, y, w(x, y))$ on the membrane surface, and after traversing in air a distance L reaches the point $\mathbf{X}_L = \mathbf{X}_0 + \mathbf{k}_r L$, so that (from now on we do not write the explicit dependence on (x, y) of w and of $\mathbf{k}_r$)

$$z_L = w + k_{rz} L, \tag{16}$$

and

$$x_L = x + \frac{k_{rx}}{k_{rz}} (z_L - w), \tag{17a}$$

$$y_L = y + \frac{k_{ry}}{k_{rz}} (z_L - w). \tag{17b}$$

The phase at (x_L, y_L, z_L) is thus

$$\phi_L = \phi_0 + \frac{2\pi}{\lambda} \left(n_f w + \frac{z_L - w}{k_{rz}} \right), \tag{18}$$

where ϕ_0 is the phase of the front at $z = 0$, and λ is the wavelength in air.

From (18) we can determine the z_W position of a wavefront of given phase ϕ_W as

$$z_W = w \left(1 - n_f k_{rz}\right) + k_{rz} \frac{\lambda}{2\pi} (\phi_W - \phi_0), \tag{19}$$

to which correspond the (x_W, y_W) coordinates

$$x_W = x + k_{rx} \left[\frac{\lambda}{2\pi} (\phi_W - \phi_0) - n_f w \right], \tag{20a}$$

$$y_W = y + k_{ry} \left[\frac{\lambda}{2\pi} (\phi_W - \phi_0) - n_f w \right]. \tag{20b}$$

These two relations can in principle be solved to give

$$x = x(x_W, y_W), \tag{21a}$$

$$y = y(x_W, y_W), \tag{21b}$$

which if replaced in (19) give the wavefront geometry: $z_W = z_W(x_W, y_W)$.

If this wavefront is analyzed at a position z_A we can, without loss of generality, take this position as that of the image of the origin, $x = y = 0$: $z_A = w_0 \left(1 - n_f k_{rz0}\right) + k_{rz0} \frac{\lambda}{2\pi} (\phi_W - \phi_0)$, where $w_0 = w(0, 0)$ and $k_{rz0} = k_{rz}(0, 0)$, so that

$$\frac{\lambda}{2\pi} (\phi_W - \phi_0) = \frac{z_A - w_0 \left(1 - n_f k_{rz0}\right)}{k_{rz0}}, \tag{22}$$

and analyze the deviation from a plane front: $\Delta z_W = z_W - z_A$, which is conveniently written as

$$\Delta z_W = w \left(1 - n_f k_{rz}\right) - \frac{k_{rz}}{k_{rz0}} w_0 \left(1 - n_f k_{rz0}\right) + \left(\frac{k_{rz}}{k_{rz0}} - 1 \right) z_A. \tag{23}$$

The corresponding (x_W, y_W) coordinates are written as

$$x_W = x + \frac{k_{rx}}{k_{rz0}} \left[z_A - w_0 - n_f k_{rz0} (w - w_0) \right], \tag{24a}$$

$$y_W = y + \frac{k_{ry}}{k_{rz0}} \left[z_A - w_0 - n_f k_{rz0} (w - w_0) \right]. \tag{24b}$$

In this way, Eqs. (23) and (24) give the wavefront geometry, analyzed at $z = z_A$, parameterized in terms of the (x, y) coordinates on the plane at $z = 0$.

We further model the wave-front analyzer at $z = z_A$ as having a circular aperture of radius r_A so that the section of the wave-front $\Delta z_W\left(x_W, y_W\right)$ to be studied is expressed as $\Delta z_W\left(r_A\xi\cos\phi, r_A\xi\sin\phi\right)$, with $0 \leq \xi \leq 1$, and decomposed in Zernike polynomials in polar coordinates $Z_n\left(\xi, \phi\right)$,

$$\Delta z_W = \sum_n a_n Z_n\left(\xi, \phi\right), \tag{25}$$

with

$$a_n = \frac{1}{\pi}\int_0^{2\pi}\int_0^1 \Delta z_W\left(r_A\xi\cos\phi, r_A\xi\sin\phi\right) Z_n\left(\xi, \phi\right)\xi d\xi d\phi. \tag{26}$$

We have followed the standard OSA/ANSI indexing and normalization scheme, used in the Shack-Hartmann wave-front sensor, for which the first 15-term orthonormal Zernike circle polynomials are:

$$\begin{aligned}
Z_0 &= 1,\\
Z_1 &= 2\xi\sin\phi,\\
Z_2 &= 2\xi\cos\phi,\\
Z_3 &= \sqrt{6}\xi^2\sin 2\phi,\\
Z_4 &= \sqrt{3}\left(2\xi^2 - 1\right),\\
Z_5 &= \sqrt{6}\xi^2\cos 2\phi,\\
Z_6 &= \sqrt{8}\xi^3\sin 3\phi,\\
Z_7 &= \sqrt{8}\left(3\xi^3 - 2\xi\right)\sin\phi,\\
Z_8 &= \sqrt{8}\left(3\xi^3 - 2\xi\right)\cos\phi,\\
Z_9 &= \sqrt{8}\xi^3\cos 3\phi,\\
Z_{10} &= \sqrt{10}\xi^4\sin 4\phi,\\
Z_{11} &= \sqrt{10}\left(4\xi^4 - 3\xi^2\right)\sin 2\phi,\\
Z_{12} &= \sqrt{5}\left(6\xi^4 - 6\xi^2 + 1\right),\\
Z_{13} &= \sqrt{10}\left(4\xi^4 - 3\xi^2\right)\cos 2\phi,\\
Z_{14} &= \sqrt{10}\xi^4\cos 4\phi,
\end{aligned}$$

2. Spectral response

In order to characterize the spectral response of the polydimethylsiloxane (PDMS type) elastic membrane used to fabricate the fluidic lenses, we incorporate an empirical expression for the refractive index of PDMS Sylgard 184, as reported in [10]. The refractive index $n(\lambda)$ is decreasing for increasing wavelength λ, which is typical of glass and polymeric materials. For the approximation of the dispersion across the entire visible light spectrum, the Sellmeier dispersion model is used, which describes the empirical relation between the refractive index $n(\lambda)$ and the wavelength λ, given by:

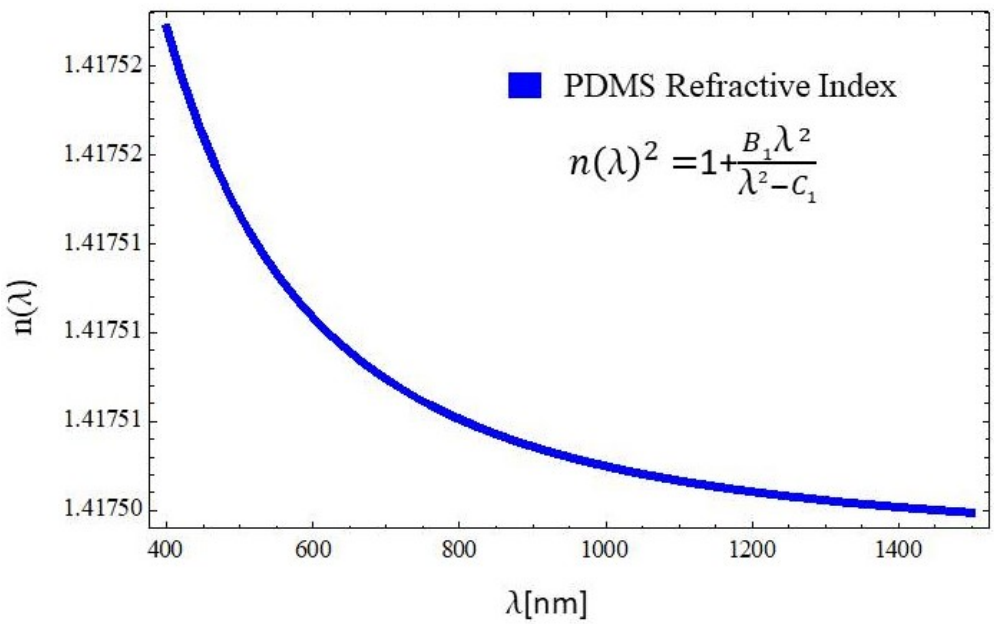

Fig. 3. PDMS refractive index ($n(\lambda)$) vs. wavelength (λ). The refractive index is obtained by experimentally determining the Sellmeier coefficients (B_1, C_1), resulting in $n(\lambda)^2 = 1 + \frac{B_1\lambda^2}{\lambda^2 - C_1}$, with $B_1 = 1.0093$ and $C_1[nm^2] = 13.185$ [10].

$$n(\lambda)^2 = 1 + \frac{B_1\lambda^2}{\lambda^2 - C_1} + \frac{B_2\lambda^2}{\lambda^2 - C_2} + \frac{B_3\lambda^2}{\lambda^2 - C_3}, \tag{27}$$

where $B_1, B_2, B_3, C_1, C_2, C_3$ are the experimentally determined Sellmeier coefficients. As reported in Ref. [10], $B_1 = 1.0093$ and $C_1[nm^2] = 13.185$. Due to the limited number of measurement points (three wavelengths with eight measurements each) the second and third Sellmeier coefficients are set to zero [10]. A plot of the refractive index vs. wavelength within the range 400 nm to 1500 nm is presented in Figure 3.

According to the theoretical model, the spectral response of the phase $P(x, y, \lambda)$ acquired by the beam upon propagation over a distance z_d can be expressed as:

$$P(x, y, \lambda) = \frac{2\pi}{\lambda}[n(\lambda) * w + (z_d - w) * k_z(\lambda)], \tag{28}$$

where w is the local displacement in the z-direction, and k_z is given by:

$$k_z(\lambda) = \frac{1 + (w_x^2 + w_y^2)}{n(\lambda)(w_x^2 + w_y^2) + \sqrt{1 + (1 - n(\lambda)^2)(w_x^2 + w_y^2)}}. \tag{29}$$

We performed numerical simulations of the phase acquired by the beam upon propagation over a distance $z_d = 3.5$ cm. Numerical simulations are displayed in Figure 4. Density plots of $P(x, y)$ for $\lambda = 600$ nm are displayed in Figures 4 (a) and (c). Figures 4 (b) and (d) display the corresponding contour plots. Simulations are reported for fluidic lenses with circular apertures (Top row: circular aperture with horizontal and vertical axes $a = b = 1.7$ cm), and for fluidic

lenses with elliptic apertures (Bottom row: elliptic aperture with horizontal and vertical axes $a = 1.3$ cm and $b = 1.7$ cm).

2.1. Wave-front aberrations of a single membrane

In order to characterize numerically the spectral response of optical aberrations and compare directly with experimental data, we expanded the wave-front aberrations of a single elastic membrane in terms of Zernike polynomials up to order 14, for a beam with wavelength (λ) in the range 400 − 1500 nm, thus numerically characterizing the spectral response in the visible and infrared domains. Even though we analyze wavefront aberrations in terms of Zernike polynomials up to order 14, we only display those coefficients for Zernike polynomials which are not negligible. Namely, P_0, P_2, P_3, P_6 (for circular apertures) and P_0, P_2, P_3, P_5 (for elliptic apertures). The remaining Zernike coefficients are all below 10^{-14}, for this reason they are not displayed in the figures.

Numerical results of wave-front aberrations for fluidic lenses with circular aperture (axes $a = b = 1.7$ cm) are displayed in Figure 5. Figures 5 (a), (b), (c) and (d), correspond to normalized Zernike coefficients for polynomials of orders P_0, P_2, P_3, P_6, respectively. The remaining polynomials are not reported because their coefficients are negligible ($<< 10^{-14}$). Numerical results for chromatic response of fluidic lenses with elliptic apertures characterized by

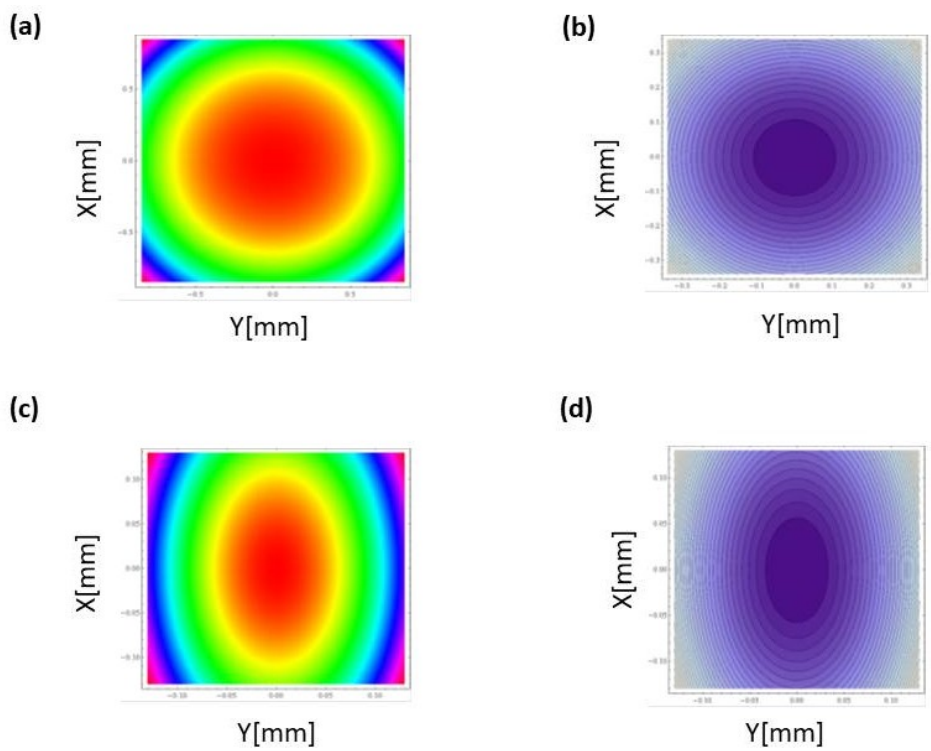

Fig. 4. (a) and (c) Density plots of acquired phase $P(x, y)$ upon propagation over a distance $z_d = 3.5$ cm, for $\lambda = 600$ nm. (b) and (d) corresponding contour plots. Top row: circular aperture with horizontal and vertical axes $a = b = 1.7$ cm. Bottom row: elliptic aperture with horizontal and vertical axes $a = 1.3$ cm and $b = 1.7$ cm, respectively.

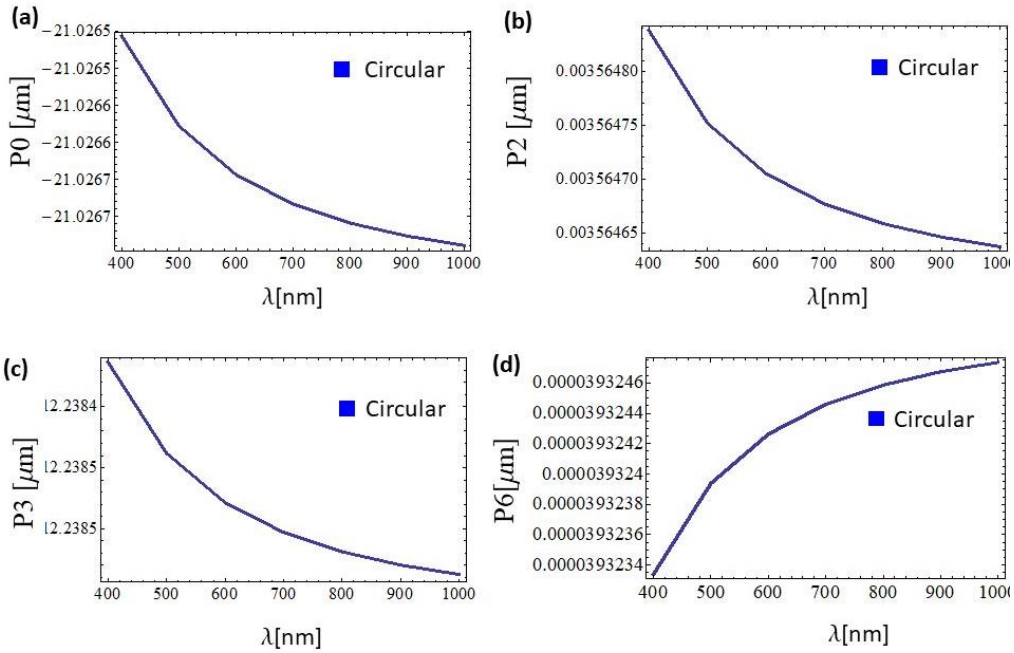

Fig. 5. Numerical simulations of optical aberrations based on the expansion of the wave-front in terms of Zernike polynomials over the visible range $\lambda = 400 - 1500$ nm, for fluidic lenses with circular aperture characterized by axes ($a = 1.7$ cm, $b = 1.7$ cm) (a), (b), (c) and (d), correspond to Zernike coefficients in $[\mu m]$ for polynomials of orders P_0, P_2, P_3, P_6, respectively. Zernike coefficients characterizing the remaining polynomials are negligible ($<< 10^{-14}$). Further details are in the text.

ellipse axes ($a = 1.5$ cm, $b = 1.7$ cm) and ($a = 1.3$ cm, $b = 1.7$ cm) are displayed in the Figure 6 and 7, respectively. Figure 6 and 7 (a), (b), (c) and (d), correspond to Zernike coefficients for polynomials of orders P_0, P_2, P_3, P_5, respectively. The remaining polynomials are not displayed because their coefficients are negligible. As it is apparent from numerical results, dependence of wave-front aberrations are of the general form $|1/\lambda|$. Moreover, spectral fluctuations in wave-front aberrations are within a fraction of λ.

Fluidic Lens Prototype

As readily reported in a previous publication [7], the fluidic lens consists of two layers of elastic membrane of the polydimethylsiloxane (PDMS) type. The two elastic films are held together by an aluminum frame, sealed with the elastic membrane. An optical fluid of refractive index matched to the polymer such as glycerol or distilled water, is injected between the elastic layers. By increasing or decreasing the fluid volume mechanically injected, it is possible to tune the focal distance across several centimeters, and adjust the optical power of the lens. Further, we tune one additional degree of freedom, given by the shape of the aperture. By modifying the aperture shape from circular (Fig. 8 (b)) to elliptical (Fig. 8 (c)), we can introduce different optical corrections. Typical size for the circular lens is given by a diameter d=17mm, the elliptic lenses have a mayor axis $b = 17$ mm, and minor axes $a = 15$ mm and $a = 13$ mm. Further details regarding the fabrication of the fluidic lens prototype are reported in a previous article [7].

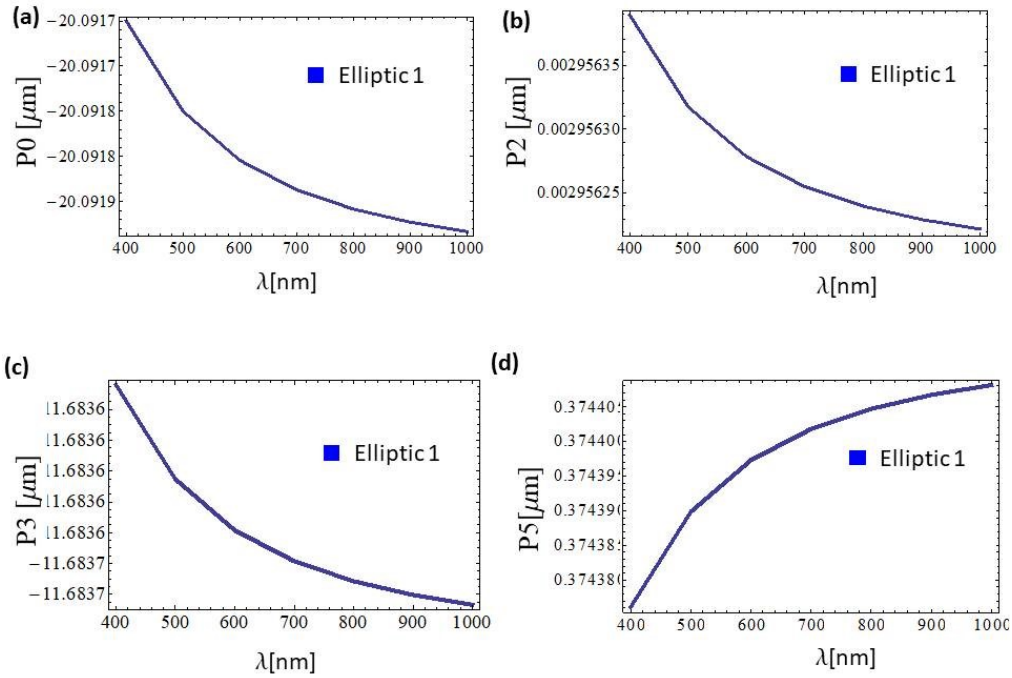

Fig. 6. Numerical simulations of optical aberrations based on the expansion of the wave-front in terms of Zernike polynomials over the visible range $\lambda = 400 - 1500$ nm, for fluidic lenses with elliptic aperture characterized by axes ($a = 1.5$ cm, $b = 1.7$ cm) (a), (b), (c) and (d), correspond to Zernike coefficients in $[\mu m]$ for polynomials of orders P_0, P_2, P_3, P_5, respectively. Zernike coefficients characterizing the remaining polynomials are negligible ($<< 10^{-14}$). Further details are in the text.

Experimental Results

2.2. Wave-front reconstruction

In order to characterize the chromatic response of the light field transmitted by the fluidic lenses, we reconstructed the wave-front transmitted through the lenses using a Shack-Hartmann wave-front sensor Fig. 8 (a) (Model Thorlabs WFS150-5C, raw experimental data can be found at our Github repository [27].). To this end, we used a collimated incoherent RGB LED source (RGB: Red-Green-Blue). Perfect collimation of a polychromatic beam can never be achieved. Here by collimation we refer to the fact that we verified the beam size did not diverge significantly over large distances (3 m or more), and we also confirmed that the wavefront impinging on the fluidic lenses was nearly a plane wavefront, so that we could use the internal calibration of the Shack-Hartmann wavefront sensor, and all measured wavefront aberrations could be ascribed to the fluidic lenses themselves.

Shack-Hartmann wavefront sensors (SHWS) enable to analyze the shape of an incident beam's wavefront by dividing the beam into an array of discrete intensity points, using a micro-lens array. These data are then used to reconstruct and analyze the shape of the wavefront using Zernike polynomials. In addition to analyzing classical optics phenomena, they are increasingly employed in applications where real-time monitoring of the wavefront is required to control adaptive optics with the intent of removing the wavefront distortion before creating an image. In particular, SHWSs enable two types of wavefront characterizations. (I) Direct measurement (not displayed

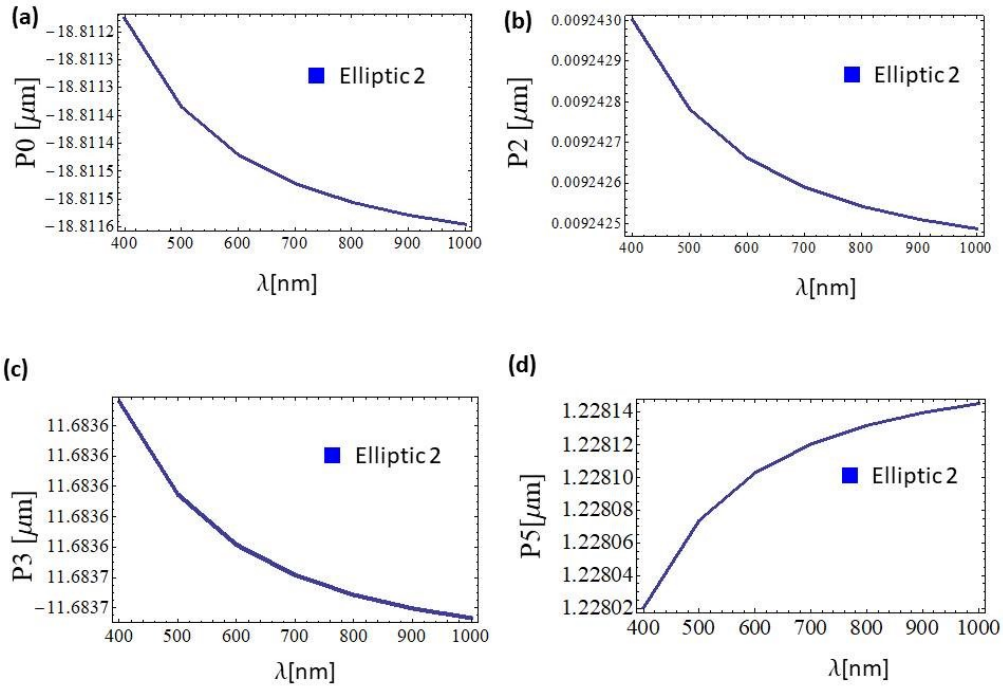

Fig. 7. Numerical simulations of optical aberrations based on the expansion of the wave-front in terms of Zernike polynomials over the visible range $\lambda = 400 - 1500$ nm, for fluidic lenses with elliptic aperture characterized by axes ($a = 1.3$ cm, $b = 1.7$ cm) (a), (b), (c) and (d), correspond to Zernike coefficients in $[\mu m]$ for polynomials of orders P_0, P_2, P_3, P_5, respectively. Zernike coefficients characterizing the remaining polynomials are negligible ($<< 10^{-14}$). Further details are in the text.

in Fig. 9): shows the wavefront which is directly calculated from the measured spot deviations using a 2-dimensional integration procedure. (II) Zernike reconstruction (left column in Fig. 9): displays the wavefront that is reconstructed using a selected set of the determined Zernike coefficients. The advantages of Zernike reconstruction are as follows: (i) Selecting only a few Zernike modes of lower order for reconstruction smooths the wavefront surface (noise canceling), (ii) the lowest order Zernike modes (for instance Z0 piston, Z1 tip and Z2 tilt) are always present but they are of less interest. Using an appropriate reconstruction (e.g., starting from Z3) can omit the Z0, Z1 and Z3 Zernike modes in order to see only the higher order modes. (iii) If selecting particular Zernike modes, they can be displayed and analyzed separately. Difference (right column in Fig. 9): displays the difference between the (I) directly measured wavefront and (II) reconstructed wavefront, and is therefore an indicator of the fit error.

The incident field had a residual field curvature below $\lambda/6$. The sensor was placed 10 cm centimeters apart from the fluidic lens, with an aperture limited by the pupil size of the sensor itself, typically 3mm diameter. We reconstructed the wave-front produced by a circular fluidic lens filled with $V_{max} = 6$ ml corresponding to an optical power (OP)= 50D (Fig. 9 (a)), and by an elliptical fluidic lens filled with $V_{min} = 4$ ml corresponding to OP=36D (Fig. 9 (c)). The qualitative difference in the wave-front due to the shape of the aperture is apparent. Residual difference between the measured wave-front and the reconstructed wave-front are displayed in Figures 9 (b) and (d). Further details on the Shack- Hartmann wave-front sensor are provided in

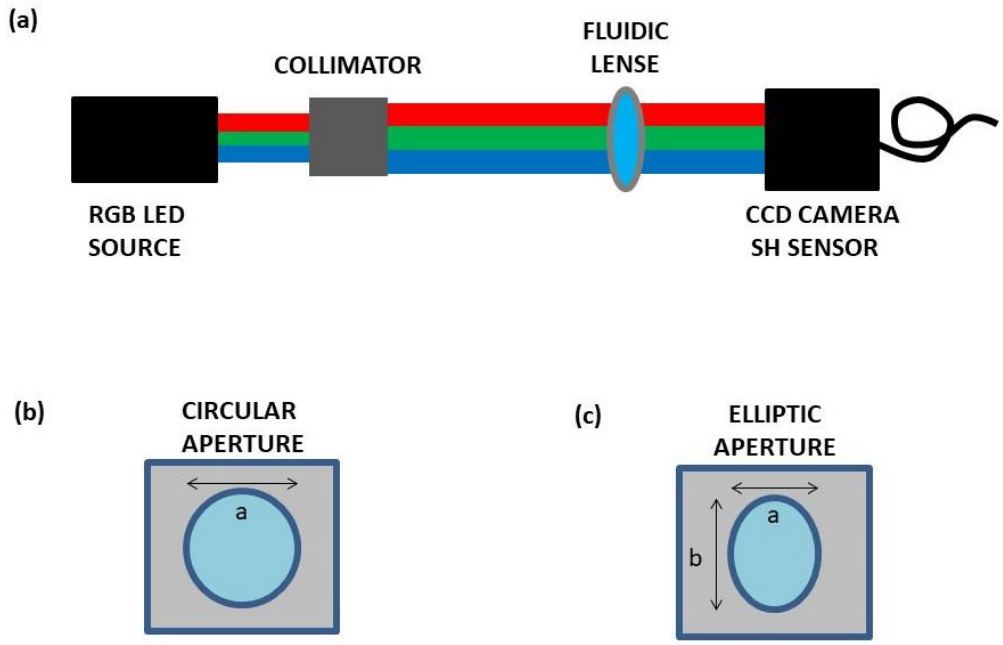

Fig. 8. Experimental scheme for reconstruction of the wave-front transmitted by the fluidic lens prototype, and characterization of the chromatic response of optical aberrations using a collimated incoherent programmable LED source (Alic Smart Life) and a Shack-Hartmann wave-front sensor (Thorlabs WFS150-5C). Scheme of fluidic-lense prototype: (b) circular aperture (horizontal and vertical axes $a = b = 17$ mm), (c) elliptic aperture (horizontal axes $(1, 2)$ $a_{1(2)} = 15(13)$ mm and vertical axis $b = 17$ mm). By tuning the aperture of the lens it is possible to address different optical aberrations.

Ref. [7].

2.3. Measured Zernike Coefficients

In order to experimentally characterize the spectral response of optical aberrations in the central region of the fluidic lens prototype, we use the experimental setup described in Fig. 8 (a). A collimated incoherent beam, produced by a programmable LED source (Alic Smart Life, 14W, Luminous Flux 1400 lm, $\lambda = 400 - 1045$ nm) propagates through the fluidic lens and is imaged by a Shack-Hartmann wave-front sensor (Model Thorlabs WFS150-5C), located at a distance of 2 cm from the fluidic lens, in order to image the near field produced by the lens. The area of the beam to be characterized is determined by the aperture of the sensor (typically 3mm). We verified that the transverse profile of the beam did not change significantly when tuning the wavelength of the source across the entire spectral range. Spectral characterizations in the visible range are mostly qualitative due to the broad spectrum produced by the incoherent LED source.

Measured aberrations in μm, in terms of the coefficients associated with Zernike polynomials of order 0 to 14, for Red, Green and Blue LED illumination are displayed in Figures 10 (a) to (i). First Column: Blue LED source, (a) Circular aperture ($a = b = 1.7$ cm), (d) Elliptic aperture 1 ($a = 1.5$ cm, $b = 1.7$ cm), (g) Elliptic aperture 2 ($a = 1.3$ cm, $b = 1.7$ cm). Second Column: Green LED source, (b) Circular aperture ($a = b = 1.7$ cm), (e) Elliptic aperture 1 ($a = 1.5$ cm, $b = 1.7$ cm), (h) Elliptic aperture 2 ($a = 1.3$ cm, $b = 1.7$ cm). Third Column: Red LED source,

(c) Circular aperture ($a = b = 1.7$ cm), (f) Elliptic aperture 1 ($a = 1.5$ cm, $b = 1.7$ cm), (i) Elliptic aperture 2 ($a = 1.3$ cm, $b = 1.7$ cm).

In order to quantify the agreement between experimental results and numerical simulations, we calculated the distance between measured Zernike coefficients for Red-Green-Blue (RGB) wavelengths. We considered three different distance measures defined for two sets of data $\{a, b, c\}$ and $\{x, y, z\}$ in the form: (1) Euclidean distance $D_1 = \sqrt{|a-x|^2 + |b-y|^2 + |c-z|^2}$, (2) Canberra distance $D_2 = |a-x|/(|a|+|x|) + |b-y|/(|b|+|y|) + |c-z|/(|c|+|z|)$, and (3) Bray-Curtis distance $D_3 = (|a-x| + |b-y| + |c-z|)/((|a+x| + |b+y| + |c+z|)$.

A brief comparison between the different distance measures is in order: D_1 corresponds to the "Pitagoric" distance, and is the only measure which can be subject to a direct geometrical interpretation, therefore in this sense it is the most intuitive one. D_2 and D_3 distance measures are similar in essence, they are both based on the algebraic concept of norm of a vector. They differ in the normalization factor, while D_2 normalizes each element of the vector independently,

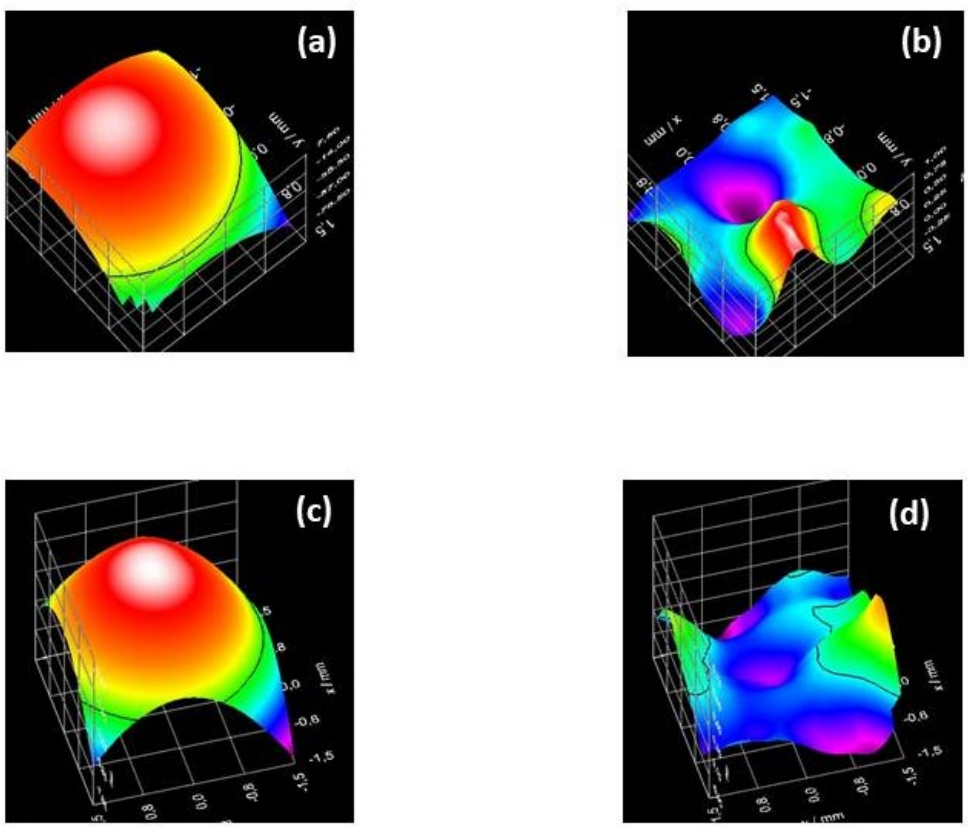

Fig. 9. Experimentally reconstructed wave-front using a Shack-Hartmann sensor (Model Thorlabs WFS150-5C) and a collimated incoherent LED source. (a) Reconstructed wave-front produced by a fluidic lens with circular aperture, (c) reconstructed wave-front produced by a fluidic lens with elliptic aperture. The qualitative difference in the wave-front due to the shape of the aperture is apparent. (b) and (d) residual difference between measured and reconstructed wave-fronts. Further details on the Shack- Hartmann wave-front sensor are provided in [7].

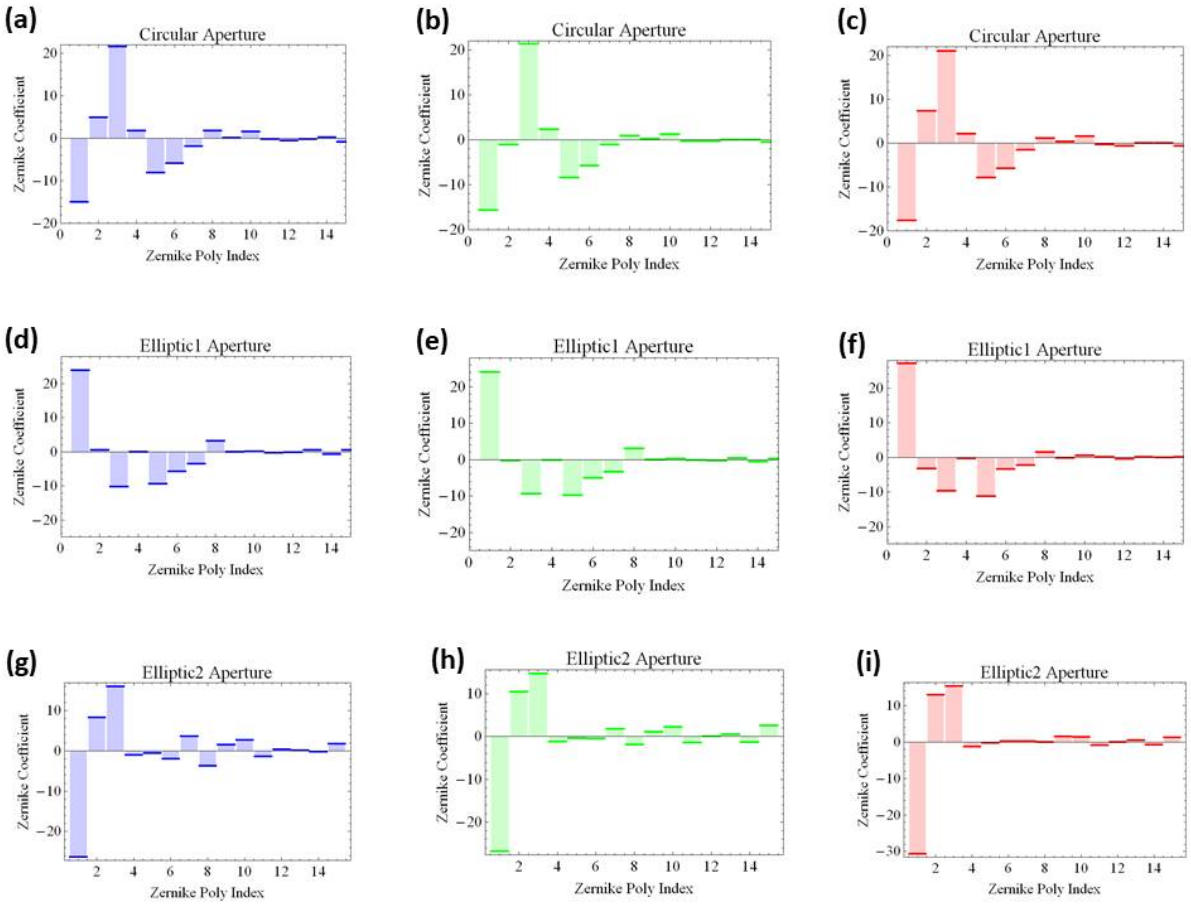

Fig. 10. (a) to (i) Measured aberrations in μm, in terms of coefficients of associated Zernike polynomials of order 0 to 14, for Blue, Green and Red LED light. First Column: Blue LED source, (a) Circular aperture ($a = b = 1.7$ cm), (d) Elliptic aperture 1 ($a = 1.5$ cm, $b = 1.7$ cm), (g) Elliptic aperture 2 ($a = 1.3$ cm, $b = 1.7$ cm). Second Column: Green LED source, (b) Circular aperture ($a = b = 1.7$ cm), (e) Elliptic aperture 1 ($a = 1.5$ cm, $b = 1.7$ cm), (h) Elliptic aperture 2 ($a = 1.3$ cm, $b = 1.7$ cm). Third Column: Red LED source, (c) Circular aperture ($a = b = 1.7$ cm), (f) Elliptic aperture 1 ($a = 1.5$ cm, $b = 1.7$ cm), (i) Elliptic aperture 2 ($a = 1.3$ cm, $b = 1.7$ cm).The agreement with numerical simulations is mostly qualitative due to the spectral broadness of the LED source. Further details are in the text.

D_3 introduces a global normalization factor, and is therefore less sensitive (larger in modulus), as it can be verified in Figure 11 (g) and (j). Note that D_1 is not normalized, for this reason it is typically larger in modulus than D_2 and D_3. We did not include the Manhattan distance in this analysis because it returned practically identical results to the Euclidean distance. The usefulness of the Manhattan measure was clearly revealed when employed in clustering techniques (see Section 2.4, Figure 12).

Comparison between spectral distances for measured Zernike coefficients in μm, for RGB wavelenghts are displayed Figure 10. Blue markers, magenta markers, and brown markers correspond to B-R distance, B-G distance and R-G distance, respectively. Figure 10 (a), (b) and (c) depict spectral distances D_1, D_2 and D_3 for fluidic lenses with circular apertures. Figures 10

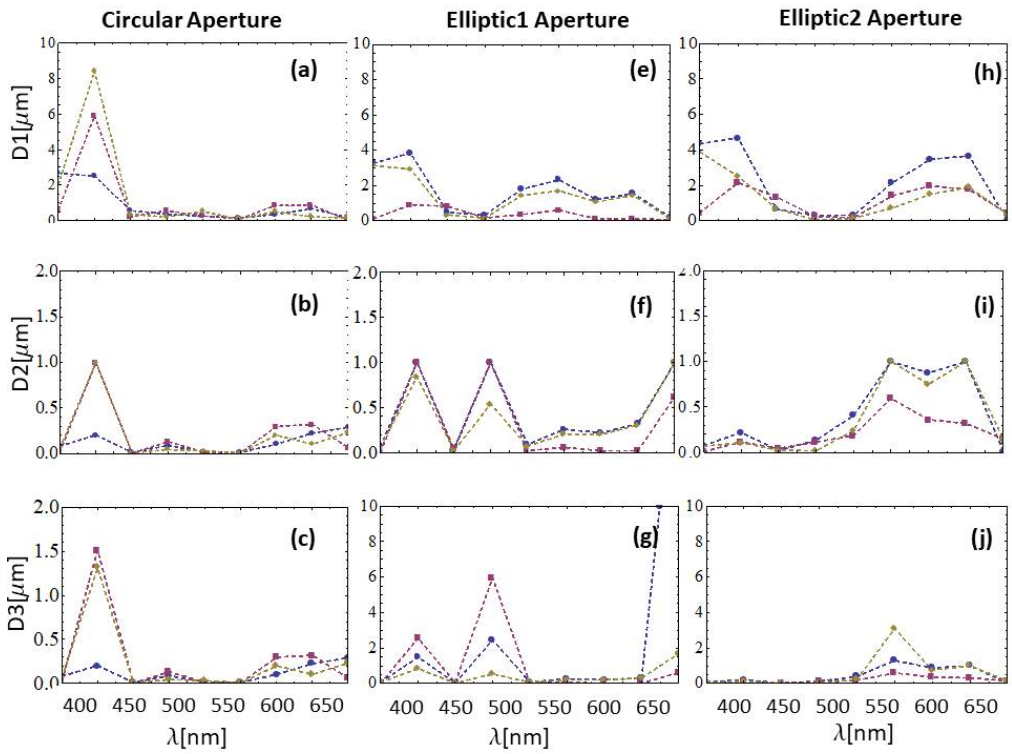

Fig. 11. Comparison between spectral distances between measured Zernike coefficients in μm, as quantified by three different distance measures D_1, D_2, D_3, for Red-Green-Blue (RGB) wavelengths. Blue markers, magenta markers, and brown markers correspond to B-R distance, B-G distance and R-G distance, respectively. (a), (b) and (c) depict spectral distances D_1, D_2 and D_3 for fluidic lenses with circular apertures. (d), (e) and (f) depict spectral distances D_1, D_2 and D_3 for fluidic lenses with elliptic 1 aperture, (g), (h) and (i) depict spectral distances D_1, D_2 and D_3 for fluidic lenses with elliptic 2 aperture. Further details are in the text.

(d), (e) and (f) depict spectral distances D_1, D_2 and D_3 for fluidic lenses with elliptic1 aperture, and Figs. 10 (g), (h) and (i) depict spectral distances D_1, D_2 and D_3 for fluidic lenses with elliptic2 aperture. Distances are within a fraction of the wavelength, in agreement with numerical simulations.

2.4. Partition into Clusters

In order to further classify the spectral response of optical aberrations, we partitioned the data into a predetermined number of clusters (N) across the visible range ($\lambda = 400 - 650$ nm). More specific, Zernike coefficients were partitioned into subgroups (or clusters) representing proximate collections of elements based on a distance or dissimilarity function. In particular, we consider the Manhattan distance, given by the sum of the absolute difference between the elements. Identical element pairs have zero distance or dissimilarity and are grouped into a given cluster, all others have positive distance or dissimilarity.

Clustering techniques provide for a robust quantitative tool to classify large sets of data according to the distance between the elements in the clusters. This, in turn, can enable to identify emerging trends in experimental data. In addition, they can enable quantitative comparisons between experiment and numerical/theoretical predictions. Moreover, in our case, we performed

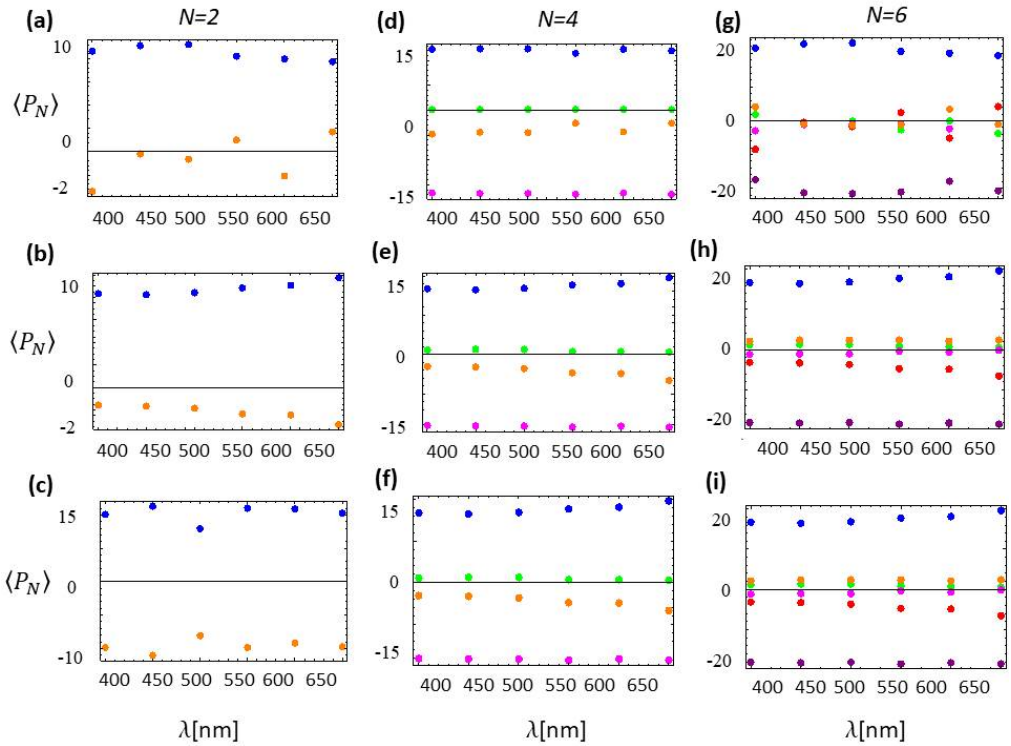

Fig. 12. (a) to (i) Experimental clusters for average Zernike coefficients ($\langle P_N \rangle$) in the range $\lambda = 400 - 650$ nm, partitioned into a predetermined set of N clusters with $N = 2, 4, 6$. First Column: $N = 2$ clusters. (a) Circular aperture ($a = b = 1.7$ cm), (b) Elliptic aperture 1 ($a = 1.5$ cm, $b = 1.7$ cm), (c) Elliptic aperture 2 ($a = 1.3$ cm, $b = 1.7$ cm). Second Column $N = 4$ clusters. (d) Circular aperture ($a = b = 1.7$ cm), (e) Elliptic aperture 1 ($a = 1.5$ cm, $b = 1.7$ cm), (f) Elliptic aperture 2 ($a = 1.3$ cm, $b = 1.7$ cm). Third Column: $N = 6$ clusters. (g) Circular aperture ($a = b = 1.7$ cm), (h) Elliptic aperture 1 ($a = 1.5$ cm, $b = 1.7$ cm), (i) Elliptic aperture 2 ($a = 1.3$ cm, $b = 1.7$ cm). Further details are in the text.

clustering techniques based on an alternative distance measure, e.g., the Manhattan distance, which provided for further insights into the way in which averaged experimental data are grouped and distributed, according to the input wavelength. For instance, from the clustering analysis one can infer that average positive and negative Zernike coefficient are typically distributed with similar probabilities, for all input wavelengths. Note that the insights provided by clustering techniques are complementary to the direct calculations of distances between elements (Figure 11).

Experimental clusters for average Zernike coefficients ($\langle P_N \rangle$) in the range $\lambda = 400 - 650$ nm, partitioned into a predetermined set of $N = 2, 4$, and 6 clusters are presented in Figures 12 (a) to (i). First Column: $N = 2$ clusters. (a) Circular aperture ($a = b = 1.7$ cm), (b) Elliptic aperture 1 ($a = 1.5$ cm, $b = 1.7$ cm), (c) Elliptic aperture 2 ($a = 1.3$ cm, $b = 1.7$ cm). Second Column $N = 4$ clusters. (d) Circular aperture ($a = b = 1.7$ cm), (e) Elliptic aperture 1 ($a = 1.5$ cm, $b = 1.7$ cm), (f) Elliptic aperture 2 ($a = 1.3$ cm, $b = 1.7$ cm). Third Column: $N = 6$ clusters. (g) Circular aperture ($a = b = 1.7$ cm), (h) Elliptic aperture 1 ($a = 1.5$ cm, $b = 1.7$ cm), (i) Elliptic aperture 2 ($a = 1.3$ cm, $b = 1.7$ cm). For $N = 2$, Zernike coefficients can be classified into two main clusters, corresponding to either an average positive amplitude $\langle P_2 \rangle = +10$ (blue dots), or

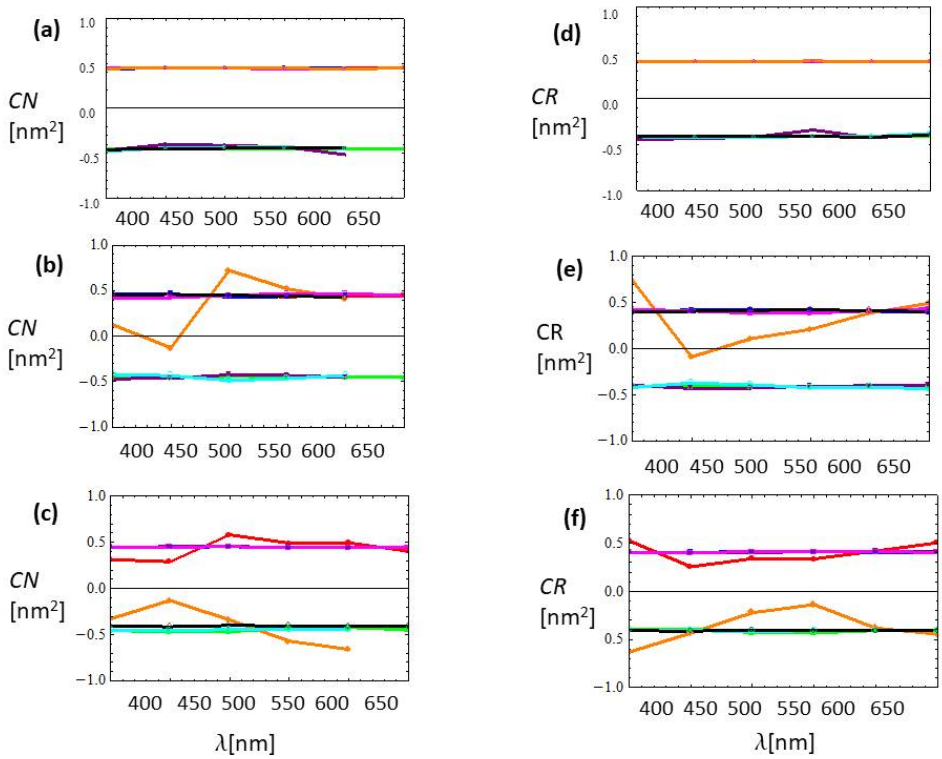

Fig. 13. (a) to (f) Normalized convolution (CN) and correlation (CR) between wavelength (λ) and measured Zernike coefficients (P_s). Left column: $CN[nm^2]$. (a) Circular aperture ($a = b = 1.7$ cm), (b) Elliptic aperture 1 ($a = 1.5$ cm, $b = 1.7$ cm), (c) Elliptic aperture 2 ($a = 1.3$ cm, $b = 1.7$ cm). Rigth column: $CR[nm^2]$. (a) Circular aperture ($a = b = 1.7$ cm), (b) Elliptic aperture 1 ($a = 1.5$ cm, $b = 1.7$ cm), (c) Elliptic aperture 2 ($a = 1.3$ cm, $b = 1.7$ cm). Further details are in the text.

an average negative amplitude $\langle P_2 \rangle = -2$ (orange dots). Next, for $N = 4$, Zernike coefficients can be classified into 4 clusters, one with an average positive amplitude $\langle P_4 \rangle = +15$ (blue dots), one with an average negative amplitude $\langle P_4 \rangle = -15$ (magenta dots), and remaining two with nearly vanishing amplitudes $\langle P_4 \rangle \approx 0$ (green and orange dots). Finally, for $N = 6$, Zernike coefficients are classified into 6 clusters, one with an average positive amplitude $\langle P_6 \rangle = +20$ (blue dots), one with an average negative amplitude $\langle P_6 \rangle = -20$ (purple dots), and the remaining 4 clusters with nearly vanishing amplitudes $\langle P_6 \rangle \approx 0$ (green, orange, magenta and red dots). The decreasing amplitude of the average Zernike coefficients for decreasing the number of clusters (N) can be ascribed to averaging over a broader range of amplitudes, since reducing N increases the diversity of the elements.

2.5. Convolution and Correlation

Convolution (CN) and correlation (CR) measurements are robust analytical tools which enable quantitative analyses of the interrelation between two experimental magnitudes. In this case, Zernike coefficients vs. wavelength. Specifically, CR/CN=+1(-1) represents a maximal positive(negative) interrelation, while CR/CN=0 represent no interrelation at all. Moreover, these methods enable to identify emerging trends, or salient features for specific values of the measured quantities. In addition, they enable direct contrast and comparison with other characterization

methods, such as clustering techniques, and with theoretical/numerical predictions. From the CR and CN data, we can conclude that the correlation between measured Zernike coefficients and wavelength is typically medium CR/CN=+0.5(-0.5), uniformly distributed between positive and negative values for all wavelength, with no specific wavelength-dependent salient features. These results are in agreement with the conclusions obtained from clustering techniques, and from numerical predictions.

In both CN and CR the basic idea is to combine a kernel list with successive sub-lists of a list of data. The convolution of a kernel K_r with a list u_s has the general form $\sum_r K_r u_{s-r}$, while the correlation has the general form $\sum_r K_r u_{s+r}$. In particular, for a kernel list $K_r = [x, y]$ and list of data $u_s = [a, b, c, d, e]$, the convolution (CN) results in the combined list:

$$CN = [bx + ay, cx + by, dx + cy, ex + dy], \tag{30}$$

while the correlation (CR) results in the combined list:

$$CR = [ax + by, bx + cy, cx + dy, dx + ey]. \tag{31}$$

We calculated the convolution (CN) and correlation (CR) between the wavelength (λ) and the measured Zernike coefficients (P_s), where $s = 0, ..., 14$ labels the polynomial order in each sub-list. We consider a kernel specified by the wavelength range $K_r = [400, 450, 500, 550, 600, 650]$ in nm, and list of measured Zernike coefficients ($P_s(\lambda)$) in nm, for each different input wavelength (λ), of the form $u_s = [P_s(400), P_s(450), P_s(500), P_s(550), P_s(600), P_s(650)]$. A plot of the normalized correlation (CR) and convolution (CN) are presented in Figures 13 (a) to (f). Left column: $CN[nm^2]$. (a) Circular aperture ($a = b = 1.7$ cm), (b) Elliptic aperture 1 ($a = 1.5$ cm, $b = 1.7$ cm), (c) Elliptic aperture 2 ($a = 1.3$ cm, $b = 1.7$ cm). Right column: $CR[nm^2]$. (d) Circular aperture ($a = b = 1.7$ cm), (e) Elliptic aperture 1 ($a = 1.5$ cm, $b = 1.7$ cm), (f) Elliptic aperture 2 ($a = 1.3$ cm, $b = 1.7$ cm). As a general trend, Zernike polynomials display either a positive correlation with λ ($CR/CN = +0.5$), or a negative correlation with λ ($CR/CN = -0.5$). Fluctuations on this trend increases as the asymmetry in the ellipse axes increases. The significant color spread indicates that there is no particular correlation, neither positive nor negative, between the Zernike order (s) and wavelength (λ).

Discussion

We have presented a comprehensive numerical and experimental study of the spectral response of optical aberrations in macroscopic fluidic lenses with high dioptric power, tunable focal distance, and aperture shape [7]. Our investigation is based on an empirical characterization of the optical and material properties of thin elastic membranes, in particular of the refractive index of polymers, such as PDMS, according to the first order Sellmeier model [10]. Using a Shack-Hartmann wave-front sensor we experimentally reconstructed the near-field wave-front transmitted by such fluidic lenses, and we characterized the chromatic response of optical aberrations in terms of Zernike polynomials over the visible wavelength range ($\lambda = 400 - 650$ nm), using an incoherent programmable LED source. Moreover, we further classified the spectral response of the lenses using clustering techniques, encountering that for a pre-determined number of clusters ($N = 2, 4, 6$), the Zernike coefficients characterizing the spectral response can be classified in three main clusters over the entire wavelength range. Namely, a cluster with positive Zernike coefficients, a cluster with negative Zernike coefficients, and a cluster with nearly vanishing Zernike coefficients. In addition we performed correlation (CR) and convolution (CN) measurements, finding that as a general trend Zernike polynomials display either a positive correlation with λ ($CR/CN = +0.5$), or a negative correlation with λ ($CR/CN = -0.5$). Fluctuations on this trend increases as the asymmetry in the ellipse axes increases. Experimental results are in agreement with our theoretical model of the non-linear elastic membrane deformation. A complete characterization

of the spectral response of optical aberrations for coherent illumination will be presented in an upcoming work.

Acknowledgements

The authors are grateful to the Solar Energy Department (TANDAR-CNEA) and to the Laboratory of Polymers (FCEN-UBA) for assistance in PDMS membrane preparation. GP gratefully acknowledges financial support from PICT2014-1543, PICT2015-0710 Startup, UBACyT PDE 2016, UBACyT PDE 2017.